120

PHYSICAL REVIEW LETTERS

Articles published week ending 29 JUNE 2018

PRL 120 (26), 260401–269901, 29 June 2018 (392 total pages)

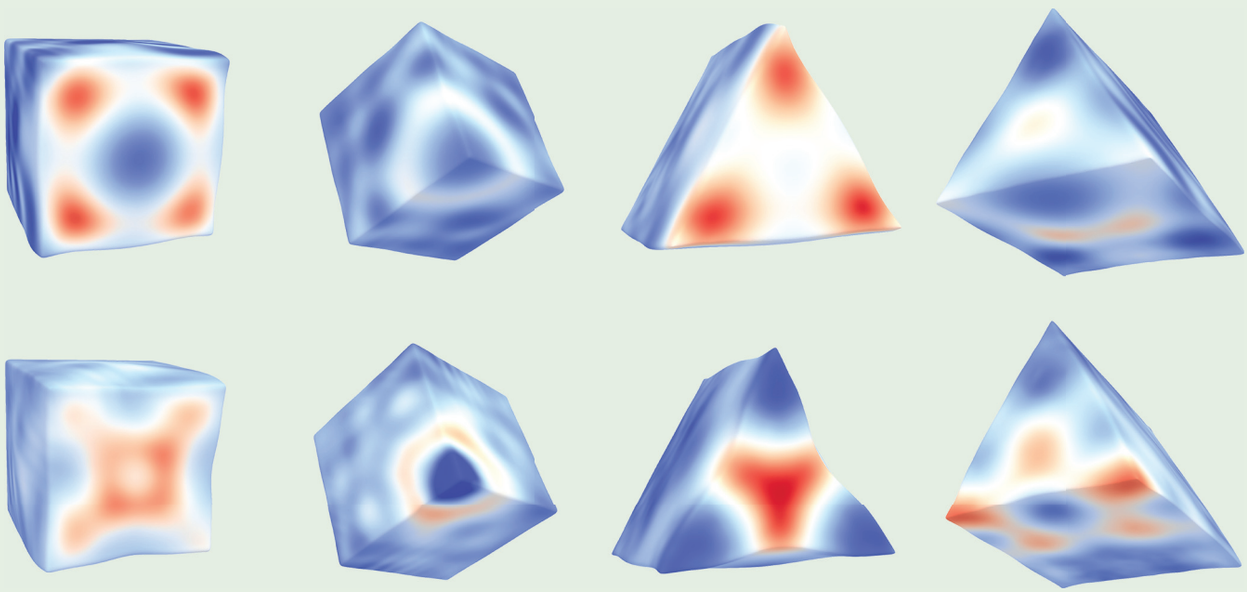

26

Published by
American Physical Society

APS physics

Volume 120, Number 26

Geometry of Wave Propagation on Active Deformable Surfaces

Pearson W. Miller, Norbert Stoop, and Jörn Dunkel
Department of Mathematics, Massachusetts Institute of Technology, 77 Massachusetts Avenue, Cambridge, Massachusetts 02139-4307, USA

(Received 5 October 2017; revised manuscript received 5 March 2018; published 29 June 2018)

Fundamental biological and biomimetic processes, from tissue morphogenesis to soft robotics, rely on the propagation of chemical and mechanical surface waves to signal and coordinate active force generation. The complex interplay between surface geometry and contraction wave dynamics remains poorly understood, but it will be essential for the future design of chemically driven soft robots and active materials. Here, we couple prototypical chemical wave and reaction-diffusion models to non-Euclidean shell mechanics to identify and characterize generic features of chemomechanical wave propagation on active deformable surfaces. Our theoretical framework is validated against recent data from contractile wave measurements on ascidian and starfish oocytes, producing good quantitative agreement in both cases. The theory is then applied to illustrate how geometry and preexisting discrete symmetries can be utilized to focus active elastic surface waves. We highlight the practical potential of chemomechanical coupling by demonstrating spontaneous wave-induced locomotion of elastic shells of various geometries. Altogether, our results show how geometry, elasticity, and chemical signaling can be harnessed to construct dynamically adaptable, autonomously moving mechanical surface waveguides.

DOI: 10.1103/PhysRevLett.120.268001

Wave propagation in complex geometries has been studied for centuries [1] in fields as diverse as optics [2], hydrodynamics [3], and gravitation [4]. The motion of a wave can be manipulated by precisely tuning the geometrical properties of its medium, an effect exploited by novel optical [5] and acoustic [6,7] metamaterials with versatile refractive properties. The problem of waveguidance becomes particularly interesting in soft active systems, where traveling waves can locally contract, shear, or otherwise deform the surfaces on which they propagate. Although most commonly seen in biological contexts [8–11], wave-induced deformation is increasingly being explored in the context of soft materials engineering [12], and there is evidence suggesting that such a deformation can exert strong feedback on the propagation of chemical waves [13–15]. Broadening our understanding of chemomechanical wave propagation is essential for the development of smart materials and soft robotics devices [16,17] that utilize chemical gradients and targeted buckling [18].

Here, we show how the complex interplay between autonomous chemical waveguidance and geometry can be used to functionalize soft active matter. Our analysis builds on a generic, broadly applicable model in which wave dynamics couples covariantly to a deformable elastic surface. We first validate the theoretical framework by replicating the behavior of contraction waves observed in recent experiment [19–21]. Subsequently, the theory is applied to design autonomously moving elastic shells of various shapes. Our results highlight that mechanical feedback can influence both the shape and speed of chemical waves, enabling significantly faster locomotion.

Our model contains two ingredients: an elastic shell described by the geometry and displacement of a two-dimensional (2D) surface ω, and a scalar concentration field c on ω equipped with wavelike dynamics. To capture the mechanics of the shell, we use the well-established Koiter model [22], in which stresses within the shell are integrated along the thickness direction. Assuming a small thickness h, the shell's mechanical configuration is then entirely described by the geometry of its middle-surface ω embedded in $\mathbb{R}^3$. Equilibrium configurations correspond to the minima of the elastic energy $\mathcal{E}_{\mathrm{KS}} = \mathcal{E}_S + \mathcal{E}_B$ with stretching and bending contributions

$$\mathcal{E}_S = \frac{Yh}{8(1-\nu^2)} \int_\omega d\omega \{(1-\nu)\mathrm{Tr}[(\mathbf{a}-\bar{\mathbf{a}})^2] + \nu[\mathrm{Tr}(\mathbf{a}-\bar{\mathbf{a}})]^2\}, \tag{1a}$$

$$\mathcal{E}_B = \frac{Yh^3}{24(1-\nu^2)} \int_\omega d\omega \{(1-\nu)\mathrm{Tr}[(\mathbf{b}-\bar{\mathbf{b}})^2] + \nu[\mathrm{Tr}(\mathbf{b}-\bar{\mathbf{b}})]^2\}. \tag{1b}$$

Here, ω denotes the deformed shell geometry characterized by the metric $\mathbf{a} = (a_{\alpha\beta})$ and curvature tensor $\mathbf{b} = (b_{\alpha\beta})$, with greek indices henceforth running from 1 to 2. $d\omega$ is the surface area element, Y the shell's Young's modulus, and ν the Poisson ratio ($\nu = 0.33$ throughout). $\bar{\mathbf{a}}$ and $\bar{\mathbf{b}}$ are metric

 © 2018 American Physical Society

and curvature tensors of the reference shell geometry $\bar{\omega}$. The shell has minimal vanishing energy if its deformed surface ω coincides with $\bar{\omega}$. Conventionally, $\bar{\omega}$ is identified with the undeformed, stress-free configuration of the shell. Active, stimulus-driven stresses can, however, be included in this framework by allowing local modifications of the reference configuration [23,24]. The surface $\bar{\omega}$ then generally becomes non-Euclidean [25,26], and the equilibrium configuration will have a nonzero energy characterized by residual stresses [27]. As a minimal model for chemomechanical coupling, we consider a concentration-dependent modification of the metric and curvature tensor of the form

$$\bar{\mathbf{a}} \to \exp(-A_C c)\bar{\mathbf{a}}, \quad \bar{\mathbf{b}} \to (1 - A_I c)\bar{\mathbf{b}}, \tag{2}$$

where coefficients A_C and A_I have the units of inverse concentration. A comparison of Eq. (2) to a bilayer shell model [23] is given in the Supplemental Material [28]. The exponential dependence of $\bar{\mathbf{a}}$ ensures a positive definite reference metric for all values of c. Consequently, $1/A_C$ is the characteristic concentration scale associated with the decay of the reference metric to its minimal value of zero. Since no such constraint is necessary for the curvature tensor, we choose a linear coupling. We note that for a reference geometry parametrized by (θ_1, θ_2), the surface element area is explicitly given by $d\bar{\omega} = \sqrt{\det(\bar{\mathbf{a}})}d(\theta_1, \theta_2)$. Thus, for $A_C c_0 \gg 1$ with c_0, a characteristic concentration scale such as the peak concentration, the stress-free state of a surface element will have an area approaching 0. Conversely, when $A_C c_0 < 1$, only a small relative change of the surface area will be induced. Similarly, the curvature coupling will tend to produce reference curvature on the same order of the original surface when $|A_I c_0| < 1$ and will produce much higher curvature when $|A_I c_0| \gg 1$.

It remains to define the dynamics of the concentration field c. In biological systems, chemical waves often feature highly idiosyncratic behavior and strong dependence on parameter choices [8]. Despite these specific and unique aspects, we expect that generic features hold in many such systems. A minimal model of chemical wave propagation is given by the telegraph equation

$$c_{tt} + \alpha c_t = \gamma^2 \nabla^2 c. \tag{3}$$

Equation (3) combines wavelike and diffusive behavior [33–35]. Specifically, parameters α and γ determine the degree of diffusivity and the wave speed, respectively. Equation (3) is implicitly coupled to the surface ω via the geometry-dependent Laplace-Beltrami operator $\nabla^2 c = (1/\sqrt{|a|})\partial_\alpha(a^{\alpha\beta}\sqrt{|a|}\partial_\beta c)$, where $|a| = \det(\mathbf{a})$. In the following, we choose γ such that the timescale associated with the wave propagation $\tau_w = L/\gamma$ is much greater than the elastic equilibration timescale $\tau_m = \sqrt{L^2\rho/\mathcal{E}_{\mathrm{KS}}}$, with ρ the material density. Separating the timescales allows for the following numerical time-stepping strategy: We discretize the deformed surface ω as well as the concentration field c by $\mathcal{C}^1$-continuous subdivision finite elements [36]. Further, throughout we consider the weak dissipation regime $\alpha = 0.001 \ll \tau_w^{-1}$ to ensure that the wave front remains coherent over observed timescales.

The solutions of Eq. (3) do not necessarily conserve the total concentration. Integrating Eq. (3) over an arbitrary, smooth, simply-connected, and closed surface gives $\ddot{\bar{c}} + \alpha\dot{\bar{c}} = 0$ for the total concentration $\bar{c}(t)$. Thus, we can choose initial conditions in which the total concentration is uniformly increasing; this flexibility is essential for closely approximating experimentally measured chemical waves (Fig. 1). Unless stated otherwise, we use a narrow 2D Gaussian as our initial condition given as $c(s, t = 0) = C_0 \exp[-(s/R)^2/(2\sigma^2)]$ and $\partial_t c(s, t = 0) = -(C_0\gamma s/\sigma^2)\exp[-(s/R)^2/(2\sigma^2)]$, where s is the arclength from the pole. These initial conditions were found to produce radially symmetric waves which maintained $c > 0$ everywhere as the wave expanded and then converged at the opposite pole (Videos 1 and 2 [28]). Note that without loss of generality, we set the amplitude $C_0 = 1$ corresponding to a trivial rescaling of c in Eq. (3) and the coupling parameters A_I, A_C. Given an initial concentration field and shell geometry, we integrate Eq. (3) using Verlet time stepping and update the reference surface via Eq. (2). The shell configuration ω is then updated assuming overdamped dynamics, with forces calculated from the gradient of the shell energy, Eqs. (1a) and (1b) [24,37]. Because of the separation of the wave and mechanical timescales, this approach ensures that the shell is very close to mechanical equilibrium at all times.

The model defined by Eqs. (1)–(3) is generic and, as such, broadly applicable. To demonstrate its validity, we use it to replicate one of the best-studied examples of contractile waves in nature: the single-cell contraction waves which occur during oogenesis in many animal species [38]. These occur shortly before the first cell division, when a contractile wave travels from the vegetal to the animal pole of the embryonic cell. Here, contraction is driven by the localization and activation of myosin motors in the actin cortex. Important model systems for the study of this process are oocytes from the starfish *Patiria miniata* and the ascidian *Ascidiella aspersa* [19,21,39] [Figs. 1(a) and 1(b), top row]. Although actin cortex mechanics have been studied in the physics community for decades, the above model supports large deformations in $\mathbb{R}^3$ and incorporates active stresses in the context of non-Euclidean shells [26].

Since the cell membrane is essentially impermeable over the wave propagation timescales, we assume that the enclosed fluid volume remains constant during the wave-induced contraction. To match our model with experiments, we, thus, augment Eq. (1) with an additional term $\mu_V(V - \bar{V})^2$ to penalize deviations of the internal volume V from the reference volume $\bar{V}$. Starting from a

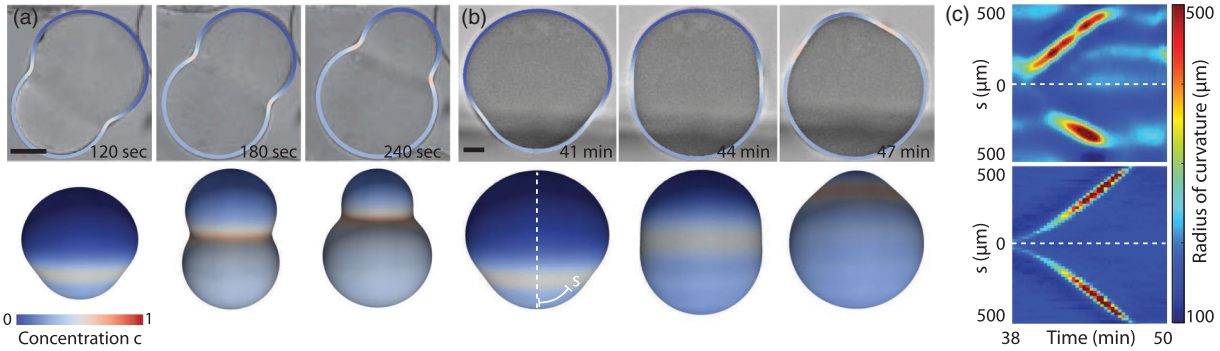

FIG. 1. Traveling wave model reproduces *in vivo* mechanics of embryonic surface contraction waves. (a) For $A_C = 1.5$ and $A_I = 1.6$, the contraction wave model reproduces sperm-triggered ascidian embryo shape dynamics. Top: Microscopy images of the deformed oocytes (adapted with permission from Ref. [19]) overlaid with cross sections of our simulation. Bottom: Corresponding 3D surfaces indicating the concentration field. Scale bar 50 μm. See Video 1 [28] for full motion. (b) Simulation with $A_C = A_I = 0.5$ reproduces the surface contraction wave in starfish oocytes during anaphase in meiosis I. Experimental images adapted with permission from Ref. [21]. Scale bar 30 μm. See Video 2 [28] for full motion. (c) Kymographs depicting the local radius of mean curvature for the experimental (top) and simulation (bottom) cases. Regions of maximal curvature indicate the center of the wave and travel at a constant speed. $\mu_V = 24Yh/R^4$, $h/R = 0.05$.

spherical oocyte shell and the initial concentration profile defined above, we tune our coupling parameters to produce local contraction and curvature of the magnitudes observed experimentally. The narrow Gaussian profile we use approximates the pointlike initial conditions observed experimentally, with $\sigma^2 = 2/R^2$ chosen to match the width of the wave in experiment. Overlaying cross sections from the elastic shell with microscopy images, we find excellent agreement between model and experiment [Figs. 1(a) and 1(b)]. We note that the wave front remains rotationally symmetric during the entire process. To gain more insights into the dynamics, we construct kymographs depicting the spatial dynamics of curvature along cross section profiles [Fig. 1(c)]. In both simulations and experiments, the wave speed is roughly constant away from the poles [constant slopes in Fig. 1(c)], suggesting only a small influence of the metric contraction on the wave propagation dynamics. Near the origin of the wave, contraction is largely in plane, effectively pulling the medium in the opposite direction of the wave propagation, while the wave maintains a constant velocity relative to local points on the surface; in the lab frame, this distortion slows its progression.

Having validated the theoretical model on spherical shells, we study implications for wave propagation in more complex archetypal geometries. Choosing a regime where the deformations are relatively small compared to the system size ($A_I = 0$, $A_C = 0.2$, $\mu_V = 0$), we simulate contraction waves on cuboid and prismatic shells keeping the same initial conditions as above but varying the location of the wave origin. We find that waves start propagating radially outward but quickly disperse due to the broken rotational symmetry of the underlying geometry. Nonetheless, they converge again at later times, on the side of the surface opposite the starting position. When they converge, they carry an imprint of the geometry of the underlying surface [Fig. 2(a)]. Since contraction is weak, this symmetry breaking can be understood as follows: In the coupling-free limit $A_C \sim A_I \to 0$, equal-time points in the wave obey the eikonal equation $|\nabla T| = \gamma^{-1}$, where γ is the wave speed above and $T(\mathbf{r})$ is the time required for the wave front to reach geodesic distance $\mathbf{r}$ from the starting point at $t = 0$ [40]. For faceted surfaces, the eikonal equation with pointlike initial conditions can be solved graphically by unwrapping the faceted surface. For the prism surface and a wave emanating from the triangle face center [Fig. 2(a), column 3], we unfold the prism around the opposite triangular face [yellow face in Fig. 2(b), top] and periodically extend the unwrapped facets. Solutions of the eikonal equation are then given as a superposition of circles centered in the origin of the wave [Fig. 2(b), top]. Comparing with simulations, we find a qualitative agreement of the incident wave patterns also for waves originating from an edge on the prism [Fig. 2(a), column 4; Fig. 2(b), bottom], suggesting that basic geometry provides the means to guide and shape surface waves. Interestingly, we find waves on the spherical shell with especially strong curvature inversion (where A_I is sufficiently high that the modified preferred radius of curvature is smaller than R by a factor of 10 or more) produce a buckling pattern which induces discrete symmetry on the sphere (Fig. S1 in the Supplemental Material [28]). Despite this change in global symmetry, we observe curvature coupling exerts minimal feedback on the propagation of waves, likely due to the isometry of curvature-induced deformation in the thin-shell limit (see the Supplemental Material [28] for further discussion). This illustrates that global geometry alone is a poor predictor of wave dynamics on an active surface.

To understand better how sustained wave dynamics interacts with geometry, deformation, and wave propagation, we consider a closed elastic shell resting on a flat surface

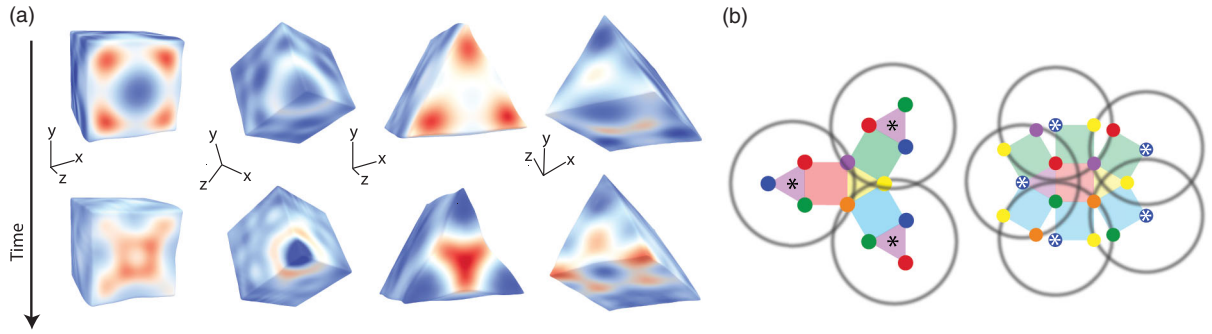

FIG. 2. For weak chemomechanical coupling, point wave propagation reflects the discrete symmetries of the elastic media. (a) Weakly coupled ($A_I = 0$, $A_C = 0.2$, side length $L = 20h$) waves propagating from a point on various geometries. On discrete surfaces, such as the cube and triangular prism shown here, self-interference increases concentration of the wave front near edges and vertices and breaks the initial radial symmetry of the wave; see Video 3 [28]. (b) Unfolded representations of the two triangular prism cases shown in (a). Through choice of starting point *, the wave front can be guided to exhibit a threefold or fivefold symmetry on the opposing face. Unique faces and vertices are color coded for clarity.

under gravity (Fig. 3). We model sustained, pulselike wave dynamics by generalizing from the telegraph Eq. (3) to FitzHugh-Nagumo dynamics [41]

$$c_t = \gamma^2 \nabla^2 c + c(1-c)(c-\nu) - w, \tag{4a}$$

$$w_t = \epsilon(c - \kappa w). \tag{4b}$$

FitzHugh-Nagumo models have been applied to describe chemical wave patterns in Belousov-Zhabotinsky reactions [42,43], which are increasingly used in active, deformable hydrogels [44]. Considering Eqs. (4), we choose parameter values within the regime of stable traveling wave solutions [41]: $\nu = -0.01$, $\kappa = 0.0001$, $\epsilon = 0.005$, and $\gamma = 0.2$. We couple c to the local metric via Eq. (2) and fix a narrow Gaussian profile as an initial condition for c_0, while $w(0) = 0$. Gravity is modeled by a constant field $\mathbf{F_g} = \rho g \hat{\mathbf{z}}$, with $g = 0.5$ in our units, and $\rho = 0.01$ is the shell surface mass density. Contact forces with the ground are described in the Supplemental Material [28].

Our simulations show that each pulse leads to a small net displacement of the entire shell in the direction of wave propagation, resulting in a persistent motion over succeeding wave cycles [Fig. 3(a)]. Remarkably, even deformations that are small relative to the system size affect the wave dynamics considerably. To demonstrate this effect, we consider a wave moving on a deforming sphere with $A_C = 0.1$, $A_I = 0$ [Fig. 3(b)] and compare with a hypothetical reference scenario in which the wave deforms the sphere but keeps propagating on the undeformed reference

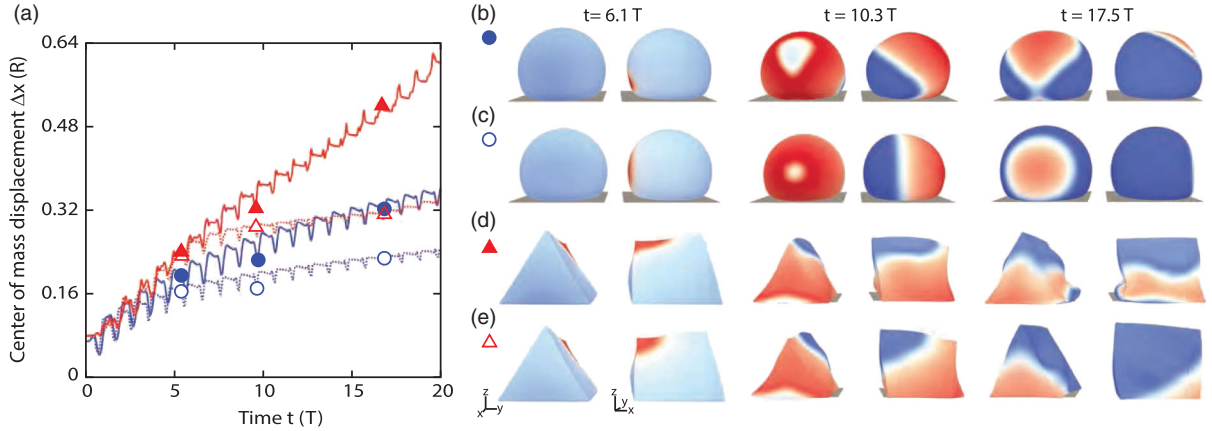

FIG. 3. Mechanically coupled chemical waves induce locomotion in elastic shells on a solid substrate under gravity; see Videos 4–7 [28]. (a) Locomotion in deformation-insensitive systems (hollow symbols, dashed lines) is slower than for deformation-coupled waves (full circles, solid lines) in spherical (blue) and prismatic shells (red). Time is normalized for each system in terms of oscillation period T, and distance is measured in terms of shell radius R. (b)–(e) Corresponding snapshots in time demonstrate that the wave shape is strongly affected by deformations (b),(d) as compared to deformation-insensitive wave propagation (c),(e). Spherical shells have radius $R = 25$, while for prisms, all edges have length $L = 2.3R$. In all cases, thickness $h = 0.084R$ and volume multiplier $\mu_V = 0.4Yh/R^4 = 11.1Yh/L^4$.

surface geometry [Fig. 3(c); Video 4 [28]]. As can be seen in Fig. 3(a), the deformation-insensitive reference sphere (blue dotted line) moves at a significantly reduced speed compared to the deformation-sensitive system (blue solid line). Thus, in this example, the mechanical feedback increases both the wave frequency and the speed of locomotion [Fig. 3(a)]. The difference between deformation-sensitive and deformation-insensitive waves becomes even more striking in our second example, where we initiate the wave with $A_C = 0.2$, $A_I = 0$ from the vertex of a triangular prism [Figs. 3(d) and 3(e)]. Specifically, in the deformation-insensitive case, we obtain a net "walking" speed of less than half that of the deformation-sensitive system [Fig. 3(a)]. Moreover, we find that the shape and propagation mode of the wave front is considerably altered due to deformation [Figs. 3(d) and 3(e); Video 5 [28]]. Additional videos showing sustained waves for other geometries and initial conditions are included in the Supplemental Material [28].

To conclude, we have shown that a generic minimal model coupling dispersive chemical wave propagation with surface elasticity can reproduce the experimentally observed surface deformation in ascidian and starfish oocytes (Fig. 1; Videos 1 and 2 [28]). It has been further demonstrated that waves confined to 3D embedded surfaces are highly susceptible to the underlying geometry of their surface (Fig. 2; Video 3 [28]), results which could be experimentally confirmed by oocytes or reconstituted actin cortices confined in shaped Polydimethylsiloxane cavities [21,45,46]. Finally, we have shown that mechanical feedback caused by wave-induced deformation likewise has a clear effect on surface wave dynamics. The presented results on wave-induced shell locomotion should provide relevant insights for the future design of autonomous Belousov-Zhabotinsky driven hydrogel actuators, which have already been shown to be capable of locomotion under externally prescribed contraction dynamics [44].

This work was supported by a National Defense Science and Engineering Graduate Fellowship (P. M.), an Alfred P. Sloan Research Fellowship (J. D.), an Edmund F. Kelly Research grant (J. D.), and a James S. McDonnell Foundation Complex Systems Scholar grant (J. D.).

[1] C. Huygens, *Traité de la Lumière* (Chez Pierre Van der Aa, Marchand Libraire, Leiden, 1885).
[2] D. Solli, C. Ropers, P. Koonath, and B. Jalali, Nature (London) **450**, 1054 (2007).
[3] J. W. M. Bush, Annu. Rev. Fluid Mech. **47**, 269 (2015).
[4] B. P. Abbott *et al.*, Phys. Rev. Lett. **116**, 061102 (2016).
[5] J. B. Pendry, D. Schurig, and D. R. Smith, Science **312**, 1780 (2006).
[6] Y. Wu, Y. Lai, and Z.-Q. Zhang, Phys. Rev. Lett. **107**, 105506 (2011).
[7] P. Wang, L. Lu, and K. Bertoldi, Phys. Rev. Lett. **115**, 104302 (2015).
[8] C. Beta and K. Kruse, Annu. Rev. Condens. Matter Phys. **8**, 239 (2017).
[9] J. Allard and A. Mogilner, Curr. Opin. Cell Biol. **25**, 107 (2013).
[10] G. Salbreux and F. Jülicher, Phys. Rev. E **96**, 032404 (2017).
[11] G. F. Oster and G. Odell, Cytoskeleton **4**, 469 (1984).
[12] L. Ionov, Mater. Today **17**, 494 (2014).
[13] N. S. Gov and A. Gopinathan, Biophys. J. **90**, 454 (2006).
[14] C.-H. Chen, F.-C. Tsai, C.-C. Wang, and C.-H. Lee, Phys. Rev. Lett. **103**, 238101 (2009).
[15] J. R. Frank, J. Guven, M. Kardar, and H. Shackleton, arXiv:1710.00103.
[16] N. Hu and R. Burgueño, Smart Mater. Struct. **24**, 063001 (2015).
[17] M. Wehner, R. L. Truby, D. J. Fitzgerald, B. Mosadegh, G. M. Whitesides, J. A. Lewis, and R. J. Wood, Nature (London) **536**, 451 (2016).
[18] J. Paulose, A. S. Meeussen, and V. Vitelli, Proc. Natl. Acad. Sci. U.S.A. **112**, 7639 (2015).
[19] M. Carroll, M. Levasseur, C. Wood, M. Whitaker, K. T. Jones, and A. McDougall, J. Cell Sci. **116**, 4997 (2003).
[20] J. Bischof, C. A. Brand, K. Somogyi, I. Májer, S. Thome, M. Mori, U. S. Schwarz, and P. Lénárt, Nat. Commun. **8**, 849 (2017).
[21] J. Bischof, Ph.D. thesis, Universität Heidelberg, 2016.
[22] P. G. Ciarlet, *An Introduction to Differential Geometry with Applications to Elasticity* (Springer, Dordrecht, Netherlands, 2005).
[23] M. Pezzulla, N. Stoop, X. Jiang, and D. P. Holmes, Proc. R. Soc. A **473**, 20170087 (2017).
[24] N. C. Heer, P. W. Miller, S. Chanet, N. Stoop, J. Dunkel, and A. C. Martin, Development **144**, 1876 (2017).
[25] Y. Klein, E. Efrati, and E. Sharon, Science **315**, 1116 (2007).
[26] E. Efrati, E. Sharon, and R. Kupferman, J. Mech. Phys. Solids **57**, 762 (2009).
[27] A. Goriely, M. Robertson-Tessi, M. Tabor, and R. Vandiver, *Mathematical Modelling of Biosystems* (Springer, New York, 2008), pp. 1–44.
[28] See the Supplemental Material at http://link.aps.org/supplemental/10.1103/PhysRevLett.120.268001 for additional examples, which includes Refs. [29–32].
[29] A. Goriely and M. Ben Amar, Phys. Rev. Lett. **94**, 198103 (2005).
[30] C. Quilliet, C. Zoldesi, C. Riera, A. Van Blaaderen, and A. Imhof, Eur. Phys. J. E **27**, 13 (2008).
[31] A. Vaziri and L. Mahadevan, Proc. Natl. Acad. Sci. U.S.A. **105**, 7913 (2008).
[32] E. Katifori, S. Alben, E. Cerda, D. R. Nelson, and J. Dumais, Proc. Natl. Acad. Sci. U.S.A. **107**, 7635 (2010).
[33] M. Kac, Rocky Mt. J. Math. **4**, 497 (1974).
[34] W. Thomson, Proc. R. Soc. A **7**, 382 (1856).
[35] J. Masoliver and G. H. Weiss, Eur. J. Phys. **17**, 190 (1996).
[36] F. Cirak, M. Ortiz, and P. Schroder, Int. J. Numer. Methods Eng. **47**, 2039 (2000).
[37] N. Stoop, R. Lagrange, D. Terwagne, P. M. Reis, and J. Dunkel, Nat. Mater. **14**, 337 (2015).

[38] A. Cheer, J.-P. Vincent, R. Nuccitelli, and G. Oster, J. Theor. Biol. **124**, 377 (1987).
[39] W. M. Bement, M. Leda, A. M. Moe, A. M. Kita, M. E. Larson, A. E. Golding, C. Pfeuti, K.-C. Su, A. L. Miller, A. B. Goryachev *et al.*, Nat. Cell Biol. **17**, 1471 (2015).
[40] K. Polthier and M. Schmies, *Proceedings of Data Visualization '99: The Joint EUROGRAPHICS and IEEE TCVG Symposium on Visualization, Vienna, Austria, 1999*, edited by E. Gröller, H. Löffelmann, and W. Ribarsky (Springer, Vienna, 1999), pp. 179–188.
[41] C. K. R. T. Jones, Trans. Am. Math. Soc. **286**, 431 (1984).
[42] W. Guo, C. Qiao, Z. Zhang, Q. Ouyang, and H. Wang, Phys. Rev. E **81**, 056214 (2010).
[43] N. J. Suematsu, T. Sato, I. N. Motoike, K. Kashima, and S. Nakata, Phys. Rev. E **84**, 046203 (2011).
[44] R. Yoshida, Adv. Mater. **22**, 3463 (2010).
[45] E. A. Shah and K. Keren, eLife **3**, e01433 (2014).
[46] T. H. Tan, M. Malik Garbi, E. Abu-Shah, J. Li, A. Sharma, F. C. MacKintosh, K. Keren, C. F. Schmidt, and N. Fakhri, Sci. Adv. **4**, eaar2847 (2018).

Supplementary Information: Geometry of wave propagation on active deformable surfaces

Pearson W. Miller, Norbert Stoop, and Jörn Dunkel
Department of Mathematics, Massachusetts Institute of Technology, 77 Massachusetts Avenue, Cambridge, MA 02139-4307, USA
(Dated: June 23, 2018)

Contact forces. Contact with the ground is modeled via a damped quadratic force:

$$\vec{F}_n = \begin{cases} (kz^2 - \beta v_z)\hat{z}, & \text{if } z \leq 0 \\ 0 & \text{otherwise} \end{cases}$$

where $k = 10.0$, the damping coefficient $\beta = 0.5$, $\hat{z}$ the unit vector in z-direction, and $v_z = \vec{v} \cdot \hat{z}$ is the normal component of the local shell velocity $\vec{v}$. For the sake of numerical stability, we approximate the Coulomb friction along this surface as

$$\vec{F}_f = -\mu |\vec{F}_n| \tanh(k_f |\vec{v}_t|) \hat{v}_t$$

where $\vec{v}_t$ is the velocity tangential to the surface, $\hat{v}_t$ a unit vector along $\vec{v}_t$, $k_f = 0.1$, and $\mu = 0.1$. These forces are applied to each point (vertex) of the discretized surface.

Symmetry breaking instability. For sufficiently strong active stresses, we expect that the wave may alter the shape and symmetries of the underlying surface significantly as it propagates. To demonstrate this effect, we consider a wave moving according to Main Text Eq. (3) on a spherical shell with large values of A_I, such that the inverted radius of curvature is much smaller than the natural radius. For this choice of coupling parameters, regions with $c \sim 1$ impose an inversion of the local preferred curvature. Since it is impossible for the shell to adopt this preferred value everywhere, we expect buckling instabilities at least within the region of large concentration c, a common phenomenon in elastic shells subject to incompatible reference configurations [1]. Indeed, we observe a series of buckling transitions with increasing n-fold symmetries as the wave propagates (Fig. S1a). The symmetry breaking bears a strong resemblance to the n-fold symmetry-breaking which arises in other buckling contexts, such as during the indentation of a spherical shell by an increasing external load [2], the isometric folding of pollen grains [3], or the buckling of colloidal particles under isotropic pressure [4]. The selection of the buckling mode results from a balance of bending and stretching energy: the more costly bending is, the fewer vertices are allowed. As such, the symmetry number n can be tuned by altering either the shell thickness h or the coupling coefficient A_I (Fig. S1b). To understand the transition between buckling modes, we note that for the above initial conditions, the intensity of the wave front will decrease as it expands over a larger surface as it travels from the pole towards the equator. Consequently, the local curvature inversion and thus the bending energy in the shell is reduced. Since the symmetry number n decreases with a decrease of bending energy, the shell passes through a series of increasing buckling modes, reaching a maximum value of n when the wave front reaches the equator. As the wave continues, it converges again towards the other side of the sphere, reverting the buckling (Movie 8).

To impose a specific symmetry, the shell has to remain fixed in a single imposed shape for an extended amount of time. This can be achieved by tuning initial conditions. Specifically, we let $c(\phi, t = 0) = [1 + \exp(-\sigma k)] \,/\, [1 + \exp(k\,[|z| - \sigma])]$ and $\partial_t c(\phi, t = 0) = -\exp(k|z|)\,[1 + \exp(k\sigma)]\, kz / (|z|\,[\exp(k\sigma) + \exp(k|z|)]\,[\exp(k\sigma) + \exp(k|z|)])$, where z is the vertical distance from the point of origin of the wave. Such a wave is a faithful representative of traveling wave fronts in reaction-diffusion systems which often maintain a constant peak concentration. As anticipated, these initial conditions support only a single symmetry mode for the duration of the wave's travel (Movie 9). Together with the results of Main Text Figs. 2 and 3, these shapes could prove sufficient to guide incoming waves; for instance, a primary wave might be employed to shape a surface to a desired symmetry, allow for properly-timed secondary waves to be dynamically guided.

Comparison to bilayer shells. The stress generation via modification of metric and curvature tensor suggested in the main text is related to a recently proposed mechanistic bilayer shell model [5]. In this model, the shell is assumed to consist of two adhering shell layers, each of which is undergoing differential volumetric expansion or contraction. Any local mismatch of the individual layer expansion then results in a net modification of the midsurface metric and curvature tensors according to

$$\bar{\mathbf{a}} \to \Lambda_c^2 \bar{\mathbf{a}}$$
$$\bar{\mathbf{b}} \to \Lambda_c \bar{\mathbf{b}} + \kappa_c \bar{\mathbf{a}}\,,$$

where Λ_c and κ_c are parameters that relate to the amount of differential swelling of the two layers [5]. As with the model used in the main text, we set $\Lambda_c^2 = \exp(-A_\Lambda c)$ and identify $A_\Lambda = A_C$ to match the concentration-dependent metric between the two models. The main difference to our proposed model is the additive modification of the reference curvature $\sim \kappa_c \bar{\mathbf{a}}$. However, for all geometries

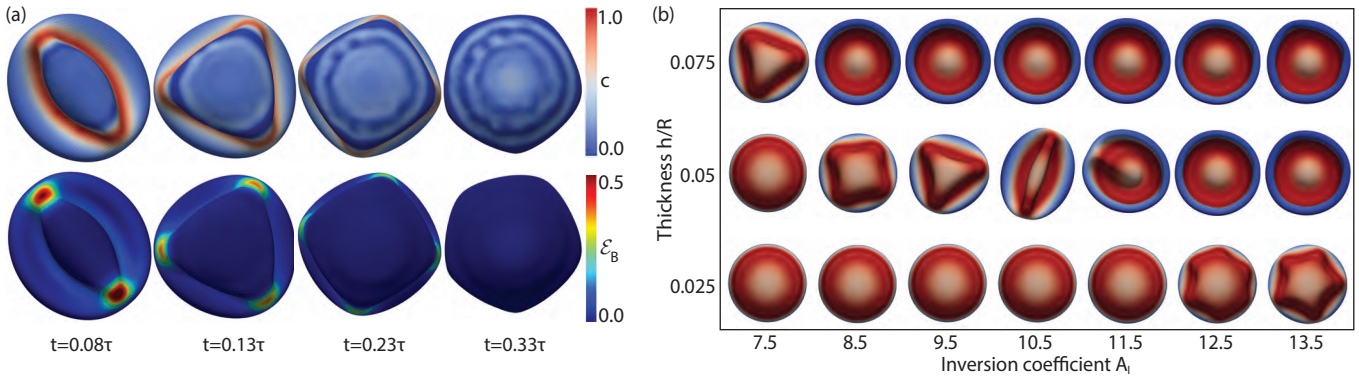

FIG. 1. Dynamical and steady-state symmetry breaking induced by chemical wave propagation with strong chemo-mechanical coupling in the absence of a volume constraint, $\mu_V = 0$. (a) Starting from a Gaussian initial profile, a wave front traveling on a sphere of radius $R/h = 20$ with $A_I = 11$ triggers a dynamical symmetry breaking transition (Movie 8). Each column represents the wave and surface at a different time t with top rows colored according to the local wave concentration and bottom rows depicting the local bending energy density $\mathcal{E}_B$, which concentrates at vertices. (b) A steady state exhibiting a single mode for the duration of the wave pulse can be produced by selecting a non-Gaussian initial condition (Movie 9). By alternating the thickness and inversion coefficient, we produce several different discrete symmetries based on the same initial condition of a point wave on a deformable sphere. Contraction coefficient $A_C = 0$ throughout. Color indicates normalized concentration.

considered, our model coincides at least approximately with the bilayer model: For spherical geometries with radius R, the curvature tensor can be simultaneously diagonalized with the metric, yielding

$$\bar{b}^{\alpha}_{\beta} = \left(\frac{1}{R\Lambda_c} + \frac{\kappa_c}{\Lambda_c^2}\right)\delta^{\alpha}_{\beta},$$

where δ^{α}_{β} is the Kronecker delta. Comparing to our model, we find that the change in preferred curvature can be matched with our model if we set

$$\kappa_c(c) = \frac{1}{R}\left[1 - A_I c - \exp\left(-\frac{A_C c}{2}\right)\right] .$$

Moreover, in all simulations on spherical geometries, $A_C c \ll 1$ for almost all time steps. Expanding the exponential, we can approximately match both models by setting $\kappa_c(c) = A_\kappa c$ with

$$A_\kappa = \frac{1}{R}\left(\frac{A_C}{2} - A_I\right).$$

For all other geometries (prisms and cubes), we note that the unmodified curvature tensor is identically to zero everywhere except the edges, where it is undefined. As such, the choice $A_\kappa = 0$ allows matching of the bilayer shell with our model. Thus, in all cases studied, the results of our model can also be interpreted mechanistically as the elastic response of a bilayer shell. In particular, locomotion under the outlined parameter matchings also arises in simulations employing the bilayer model (see Movie 10).

Movies. Movies 1 and 2 depict, respectively, simulations of the starfish and ascidian embryos discussed in Fig. 1. Movie 3 corresponds to the examples shown in Fig. 2. Movies 4 and 5 show the driven shells from Fig. 3, with the spherical and prismatic cases contained in Movies 4 and 5. Finally, Movie 6 shows locomotion of prismaitc shells with a different choice of initial conditions, and Movie 7 shows locomotion of cubic shells. Movies 8 and 9 relate to the buckling instability and are discussed above. Movie 10 demonstrates locomotion of shells actuated by chemical coupling to the bilayer shell model as defined in Ref. [5].

[1] A. Goriely and M. Ben Amar, Phys. Rev. Lett. **94**, 198103 (2005).
[2] A. Vaziri and L. Mahadevan, Proc. Natl. Acad. Sci. U.S.A. **105**, 7913 (2008).
[3] E. Katifori, S. Alben, E. Cerda, D. R. Nelson, and J. Dumais, Proc. Natl. Acad. Sci. U.S.A. **107**, 7635 (2010).
[4] C. Quilliet, C. Zoldesi, C. Riera, A. Van Blaaderen, and A. Imhof, Eur. Phys. J. E **27**, 13 (2008).
[5] M. Pezzulla, N. Stoop, X. Jiang, and D. P. Holmes, Proc. R. Soc. A **473** (2017), 10.1098/rspa.2017.0087.